

ALMA Memo No. XXX

An Imaging Study for ACA

Min S. Yun
University of Massachusetts

February 10, 2001

Abstract

1 Introduction

The ALMA Complementary Array (ACA) is one of the several new capabilities for ALMA enabled by the Japanese participation to the Project. It is conceived to be a small independent array of 6-8m diameter antennas to complement the imaging capability of the primary array of 12m diameter antennas. Its main objective is measuring the short spacing data poorly sampled by the 12m antennas. It should also be able to produce good scientific images by itself, enabling an independent, parallel observing mode, especially at higher frequencies.

There are many aspects to evaluating whether an array of 6m antennas or 8m antennas are better suited for complementing the imaging capability of the 12m antenna array (e.g. cost, calibration, seeing). In this memo, we present a set of simulated observations aimed at addressing only the uv-sampling aspects and the impact on the image construction process. The only source of “error” in this study is the sampling of the uv cells and its interaction with the imaging algorithms. The issues related to the imaging algorithms are found to be a non-trivial matter.

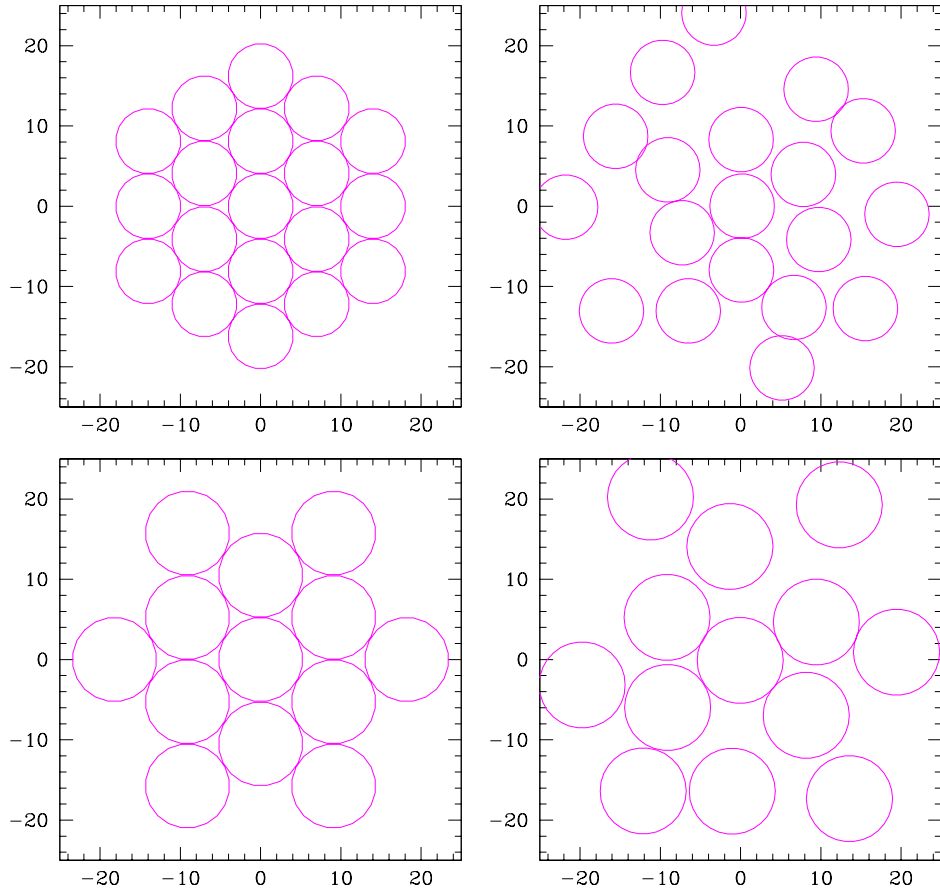


Figure 1: The ACA design layouts. The $19 \times 6m$ array is shown on top, and the $13 \times 8m$ array is shown at the bottom. The fully packed design (left) is modified for better imaging performance using the Kogan (1998) minimum sidelobe algorithm (right). Each circle represents $1.3D$ of the antennas. Axis labels are in units of meters.

2 ACA Designs

The cost and calibration considerations suggest that ACA should consist of 7 to 15 antennas of 6-8m diameter. For this study, we chose somewhat arbitrarily to compare a $19 \times 6m$ array and a $13 \times 8m$ arrays (see Table 1). While these numbers of elements are slightly on the high side, $N \geq 10$ is desirable for the good stand-alone imaging capability. Note that the mosaic imaging speed ND for the two arrays are comparable (114 vs. 104).

To achieve the best short spacing sampling, a crystalline array with $1.3D$ separation (left panels in Fig. 1) was chosen as the starting point. To

Table 1: ACA Specifications

	6m Array	8m Array	12m Array
Number of Elements	19	13	64
Diameter	40m	40m	150m
Resolution (345 GHz)	4"	4"	1"

alleviate the strong sidelobes produced by such arrays, the position of each elements are perturbed using the minimum sidelobe algorithm of Kogan (1998). After several iterations, the final configurations adopted are shown on the right panels in Figure 1.

3 Model Image and Mosaic Patterns

To evaluate the imaging capabilities properly, a large number of simulated observations involving a wide range of model images are desirable. For this study, however, we limit the simulated observations and image reconstruction to a single astronomical model image which has structures on a wide range of spatial scales. Conducting a wide range of test images is not warranted since we are only trying to test a small aspect of the ACA. A wider range of simulated observations would be desirable at a later time when the competing ACA designs are better defined.

We have selected the H α image of M51 as the test image (kindly provided to us by D. Thilker at NRAO). This test image is large ($1k \times 1k$) and has a large intrinsic dynamic range ($> 10^3$). The original image header was modified so that the whole image fits into the simulated mosaic observation field (about $2'$ in diameter at 345 GHz). The simulated images at $1''$ resolution is over-sampled by at least a factor of 4 in the original test image, ensuring that the simulated visibilities are not subject to the effects of discrete pixels in the input model.

The mosaic observations are simulated by obtaining a series of 6 minute snapshots at each pointing center for the 12m array and a series of 25 minute integrations for the 6m and 8m ACA. New visibilities are computed every 10 seconds in all cases. Since no thermal noise is included, the same weights are assigned to all visibilities, regardless of the antenna size. A greyscale

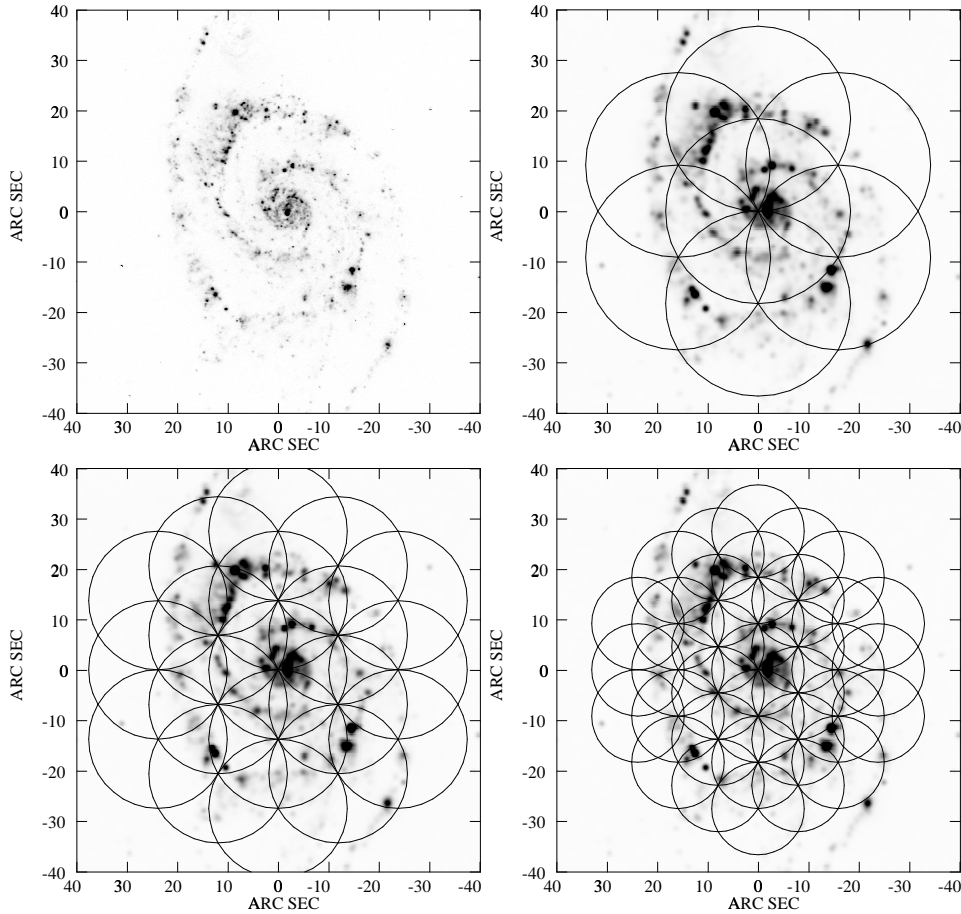


Figure 2: Model image and the mosaic footprints. A greyscale image of the raw model image is shown on top left. The mosaic footprint for the 6m (top right), 8m (bottom left), and 12m (bottom right) array are shown over the greyscale image of the model image convolved to $1''$ resolution.

representation of the input model image and the mosaic footprints for the 6m, 8m, and 12m arrays are shown in Figure 2. Traditional hexagonal mosaic pattern is chosen here for simplicity.

The total power image is obtained by convolving the input image by a Gaussian appropriate for the primary beam of the 12m antenna (18.5 arcsec at 345 GHz). Even for the imaging using the ACA alone, it is assumed that the total power data obtained using the 12m antenna array would be available.

4 Simulated Observations

Two different simulated observations are conducted: (1) ACA stand-alone; and (2) ACA + 12m array. In both cases, the simulated images with and without the total power data are obtained in order to examine the contribution of the total power data. In all cases, the total power data is essential in recovering the input model structure even though the model M51 image appears to be dominated mostly by compact sources.

To isolate the impact of the uv-sampling from the algorithmic effects, two different mosaic algorithms are tested. The AIPS routine VTESS utilizes a “maximum entropy” routine while UTESS utilizes a “maximum emptiness” routine. The convergence of the two routines are known to be somewhat source dependent. Since the model image is fundamentally all positive, however, the two routines are expected to produce fairly similar results. In both cases, the inclusion of the total power data is achieved by specifying the total power image as the “default” starting image for the iterative convergence loop.

4.1 Stand-alone Cases

The reconstructed images from the 6m and 8m antenna arrays alone are shown in Figures 3 & 5, and their difference images from the input model convolved to the corresponding resolution ($4''$) are shown in Figures 4 & 6. In both cases, inclusion of the total power data has the largest impact (i.e. top versus bottom rows), even though the input image appears to be dominated mainly by bright point sources. The algorithmic difference between maximum entropy and maximum emptiness seems minor, particularly when the images including the total power data are compared (bottom panels of Figs. 3 & 5).

The 8m antenna ACA appears to have produced qualitatively slightly better images than the 6m antenna ACA. This point is best illustrated by comparing Figures 4 & 6, which are shown using the same pixel amplitude ranges. While the peak magnitude of the differences are comparable, the spatial extents of the 8m ACA images are significantly smaller. It is possible that the distribution of spatial scales in the model image may be better matched to the 8m antenna ACA than the 6m antenna ACA, but the root cause for this difference is not well understood.

The algorithmic difference is more obvious in the comparison of images constructed without the total power data (top panels). It is entirely expected

that the (reconstructed - model) images are dominated by missing large scale structures, and the maximum emptiness algorithm (UTESS) has produced flatter images – see upper right panel in the difference images. Evidence for imaging defects seems more obvious in the maximum entropy (VTESS) images, but the image-wide DC offset introduced by the VTESS routine is responsible for the bulk of the apparent differences. The image fidelity (model \div difference) is not very different between the UTESS and VTESS images.

4.2 ACA + 12m Array

The images constructed by combining the $19 \times 6\text{m}$ ACA data and $64 \times 12\text{m}$ full array are shown in Figure 7. Unlike the stand-alone cases, the algorithmic differences between UTESS and VTESS seem relatively minor. The addition of the total power data helped to bring out the plateau of diffuse emission (lower panels). Subtle differences can be seen more clearly in the difference maps shown in Figure 8. The maximum emptiness algorithm (UTESS) resulted in a deeper and more extended negative bowl in the image produced without the total power data (top right panel) while too much flux went into the extended plateau feature when the total power is included (bottom right panel). The strong contrast associated with sharp features in the difference maps appears to be an artifact in the imaging software, unrelated to the sampling of the uv cells we are trying to test.

The images constructed by combining the $13 \times 8\text{m}$ ACA data and $64 \times 12\text{m}$ full array are shown in Figure 9. The difference images shown in Figure 10 are remarkably similar to those of the $19 \times 6\text{m}$ ACA plus $64 \times 12\text{m}$ array shown in Figure 8. Both the algorithmic and total power effects are reproduced nearly identically despite the obvious differences in the ACA components of the input data.

The spatial scales dominating the imaging errors is best determined by examining the Fourier transforms of the difference images. Greyscale representations of the real part of the Fourier transform of the difference images (Fig. 10) are shown in Figure 11. The majority of the pixels outside the $13 \text{ k}\lambda$ ($\sim 10\text{m}$) are close to zero. The upper two panels, which correspond to images constructed without the total power data, show an oval ring of negatives with a dimension of $13 \text{ k}\lambda$ ($\sim 10\text{m}$) by $7 \text{ k}\lambda$ ($\sim 5.6\text{m}$). The lower two panels are images constructed with the total power data, and they each show a positive peak of the similar dimension. Therefore the image reconstruction

errors are occurring at the same spatial scales for all cases although the flux deficit is resulted in the former cases while the flux excess is resulted in the latter.

The plot of the radial density of visibilities, shown in Figure 12, reveals that indeed the imaging errors are occurring at the spatial scales where the ACA data and the total power data are interpolated. The central pixel is close to zero in the top two panels of Figure 11, and this suggests that the mosaic imaging routine spreads out the errors evenly in the image plane. The lower panels show monotonic excess flux at low spatial frequencies, which was already noted from the direct examination of the images in Figures 7 & 9.

It appears the images constructed with the 8m ACA may be slightly better in the absence of total power data because the size of the central zero amplitude hole is slightly larger. As noted in the stand-alone cases above (see § 4.1), the true significance of this result may be marginal, however. Again, the availability of the total power dominates the resulting images, leading to a gross error in the representation of the extended structures. We conclude that *there is little substantial difference between the 6m antenna ACA and the 8m antenna ACA in terms of filling in the short spacing data (“Emerson notch”)*.

4.3 Comparison to Stand-alone $64 \times 12\text{m}$ Array

To complete the analysis of the expected ALMA imaging performance aided by the 6m ACA and 8m ACA, we now examine the expected imaging performance of the stand-alone $64 \times 12\text{m}$ array for the same test image. Cornwell, Holdaway, & Uson (1993) have argued that the full range of spatial scales can be sampled and recovered by a mosaic observation using a homogeneous array. A good imaging performance is expected for a homogeneous $64 \times 12\text{m}$ array if all conditions are ideal.

The reconstructed images and the difference images are shown in Figures 13 & 14. As was for the stand-alone 6m and 8m ACA (§ 4.1), the image reconstructed by VTESS without the benefit of the total power data has a significant DC offset while the UTESS image suffers from a deep negative bowl. Unlike the “ACA+12m array” cases (see § 4.2), the UTESS and VTESS images, constructed using the total power image as the default starting point, display significant differences. In particular, the UTESS image is quite good and comparable to the “ACA+12m array” images. On the other hand, the VTESS image is quite poor despite using the same input data, and the algorithmic dependence is brought to lighted once again.

The success of the UTess image is a verification of the homogeneous array concept proposed by Cornwell et al. (1993). On the other hand, the more limited success of the VTess algorithm represents an important warning that the data from a homogeneous array includes only just enough information and little room for error. The fact that the inclusion of the ACA data was able to drive even the VTess algorithm to a good convergence image in a robust manner is a further testimony to this warning. Given that we will face real world challenges such as decorrelation across the apertures and thermal and atmospheric noise, the ability afforded by the ACA to bridge the “Emerson notch” represents an important added insurance for assuring the robust imaging capability for ALMA.

5 Summary and Discussion

We present a set of simulated imaging studies for a $19 \times 6\text{m}$ ACA and a $13 \times 8\text{m}$ ACA, aimed at addressing the uv-sampling and the impact on the image construction process. The main goal of this study is evaluating how well the 6m and 8m antenna arrays can provide the short spacing information for a 12m antenna array. Our findings include:

- The antenna size difference (6m vs 8m) appears to have only a secondary importance in the simulated observations conducted. Reconstructed images show stronger dependence on other variables such as the inclusion of total power data and the choice of imaging algorithm.
- We confirm that total power data is extremely important in recovering the true source structures even for a source such as M51 where much of the flux is associated with compact components.
- The merit of the homogeneous array concept is verified at least in part by our imaging study of the stand-alone 12m array. At the same time, its vulnerability and little margin for error are also demonstrated. The ability afforded by the ACA to bridge the “Emerson notch” offers added robustness to the imaging capability of ALMA.

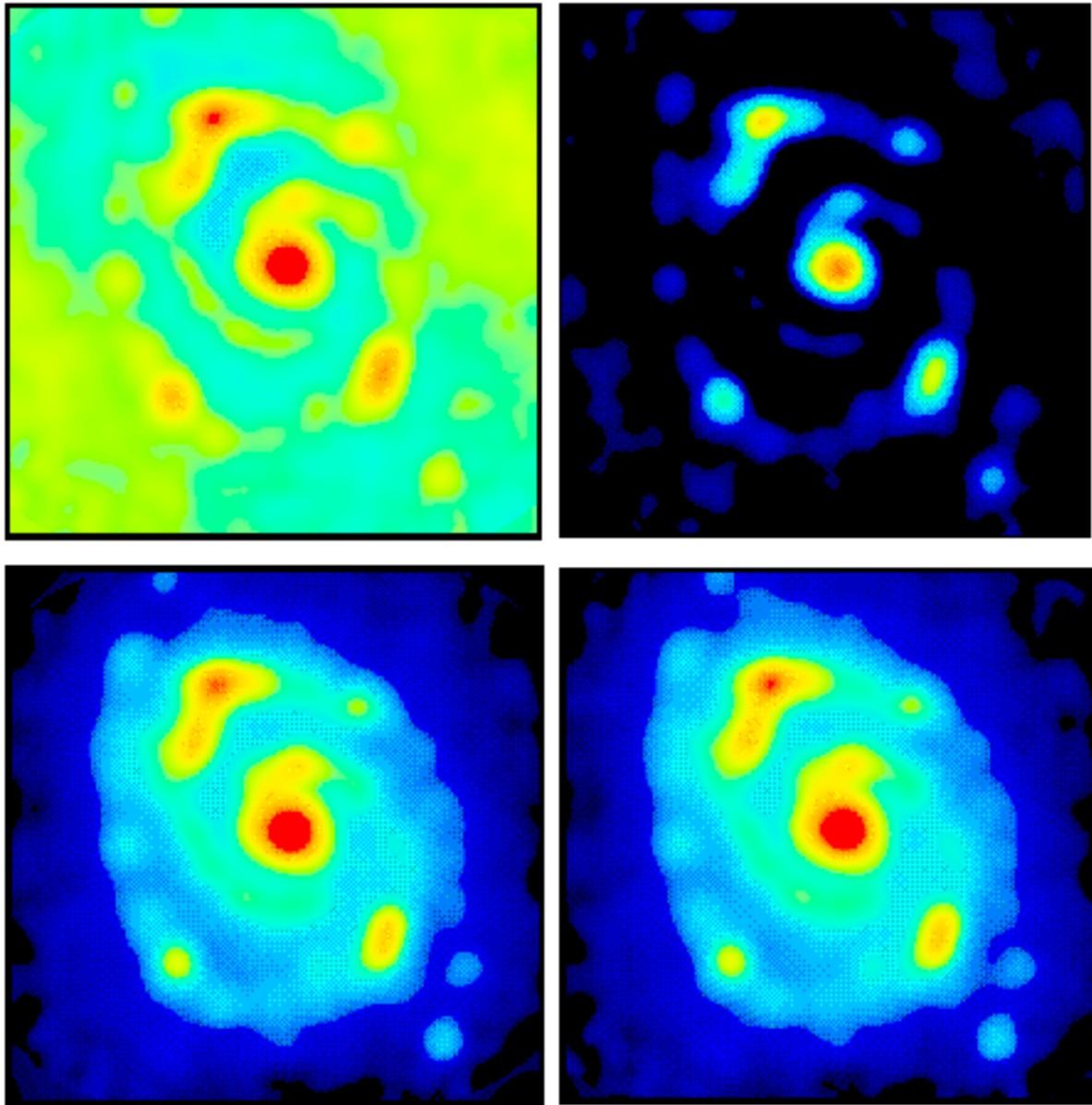


Figure 3: Simulated observations with a $19 \times 6\text{m}$ Array alone. The top row of images are produced using only the cross-correlation data only while the bottom row images include the total power data as well. The left panel images are produced using AIPS task VTESS (“maximum entropy”) while the right panel images are produced using AIPS task UTESS (“maximum emptiness”). The range of amplitude plotted are from 0 (black) to +1500 (red).

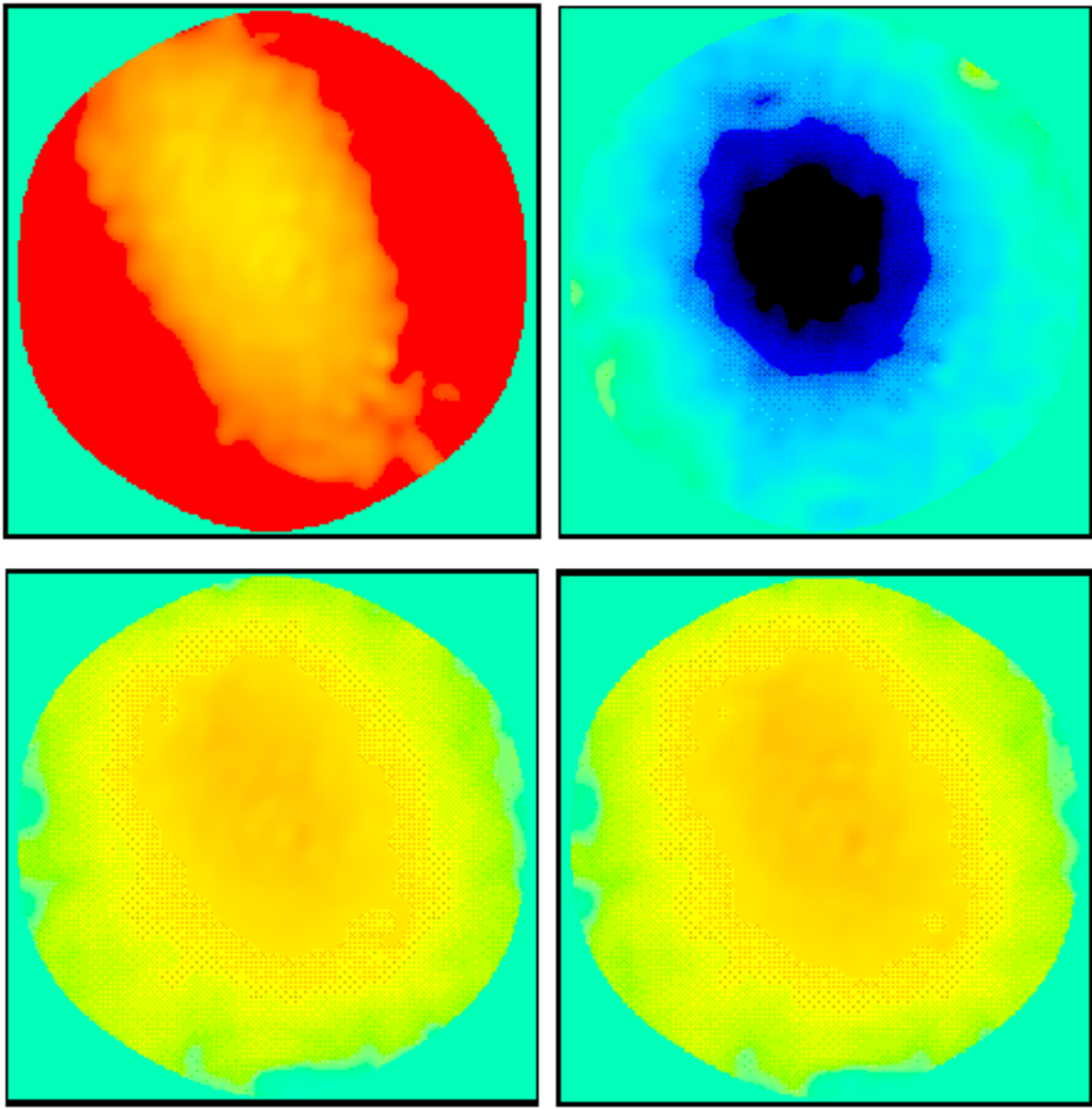


Figure 4: Difference images between the simulated observations using a 19 x 6m Array alone and the input model image convolved to the matching resolution ($4''$). The four panels correspond exactly to the images shown in Figure 3. The range of amplitude plotted are from -300 (black) to +500 (red).

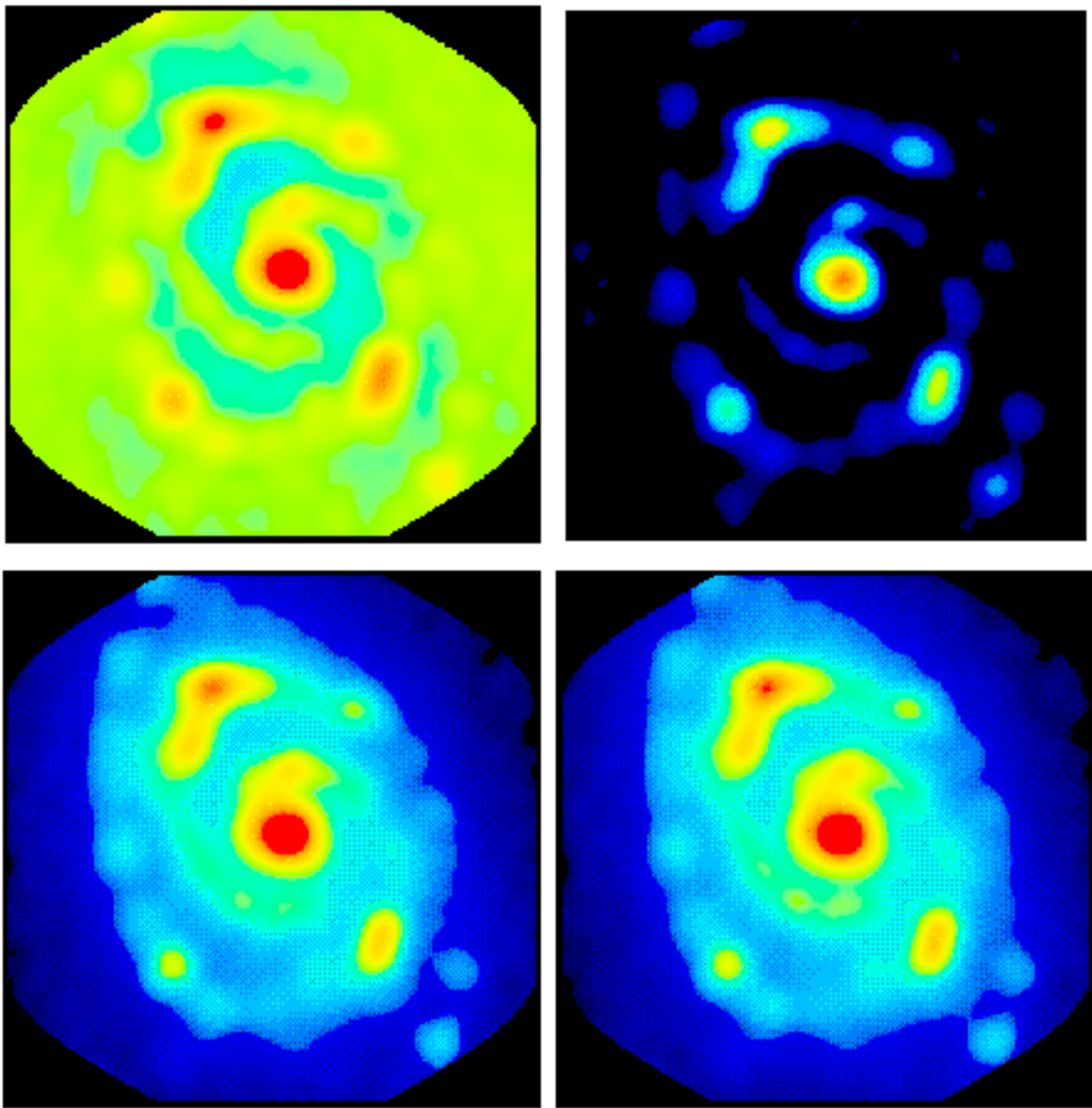


Figure 5: Simulated observations with a 13×8 m Array alone. See Figure 3 caption for the description of each panels. The range of amplitude plotted is also identical to Figure 3.

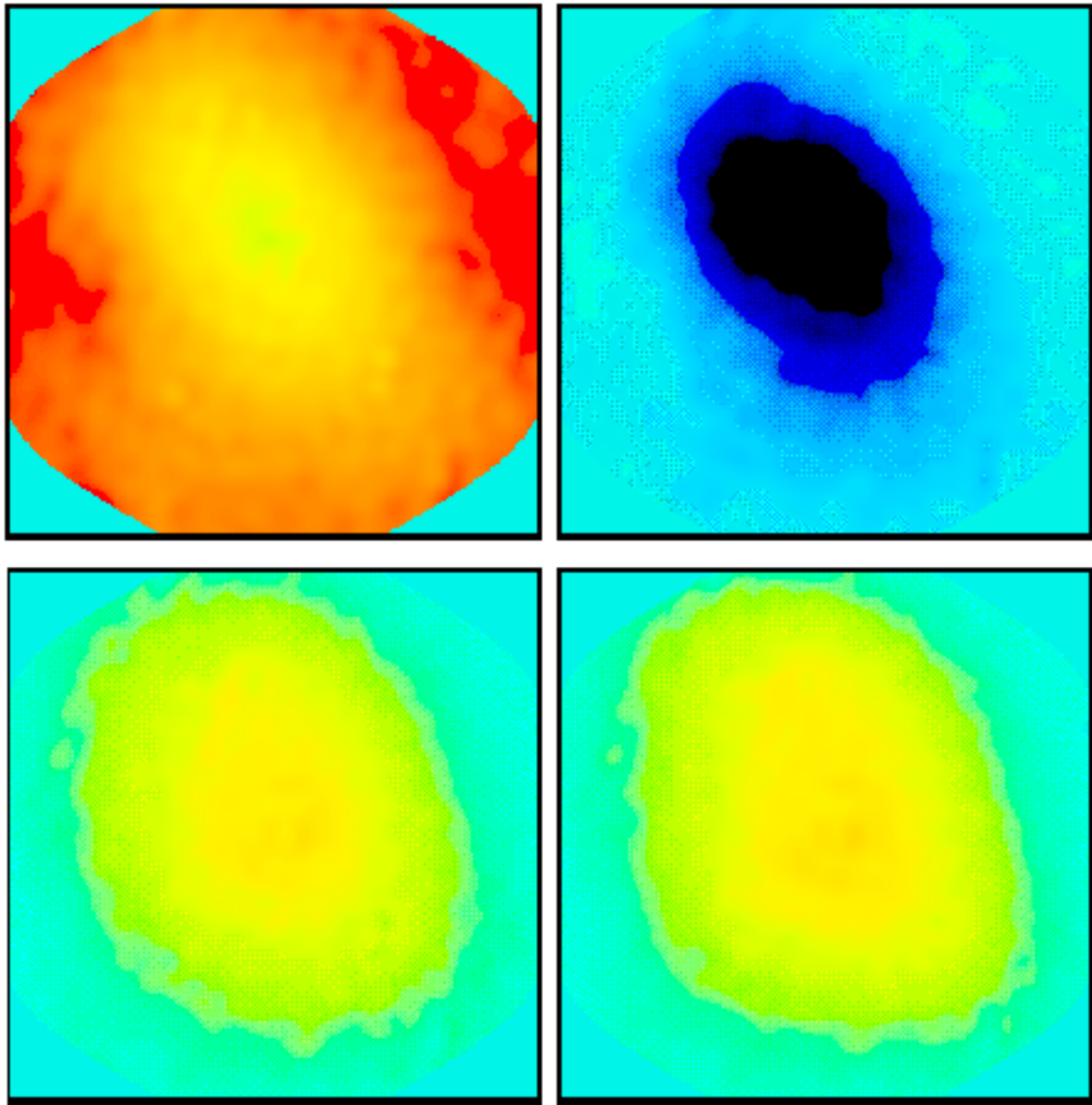


Figure 6: Difference images between the simulated observations using a 13×8 m Array alone and the input model image convolved to the match resolution ($4''$). See Figure 3 caption for the description of each panels. The range of amplitude plotted is also identical to Figure 4.

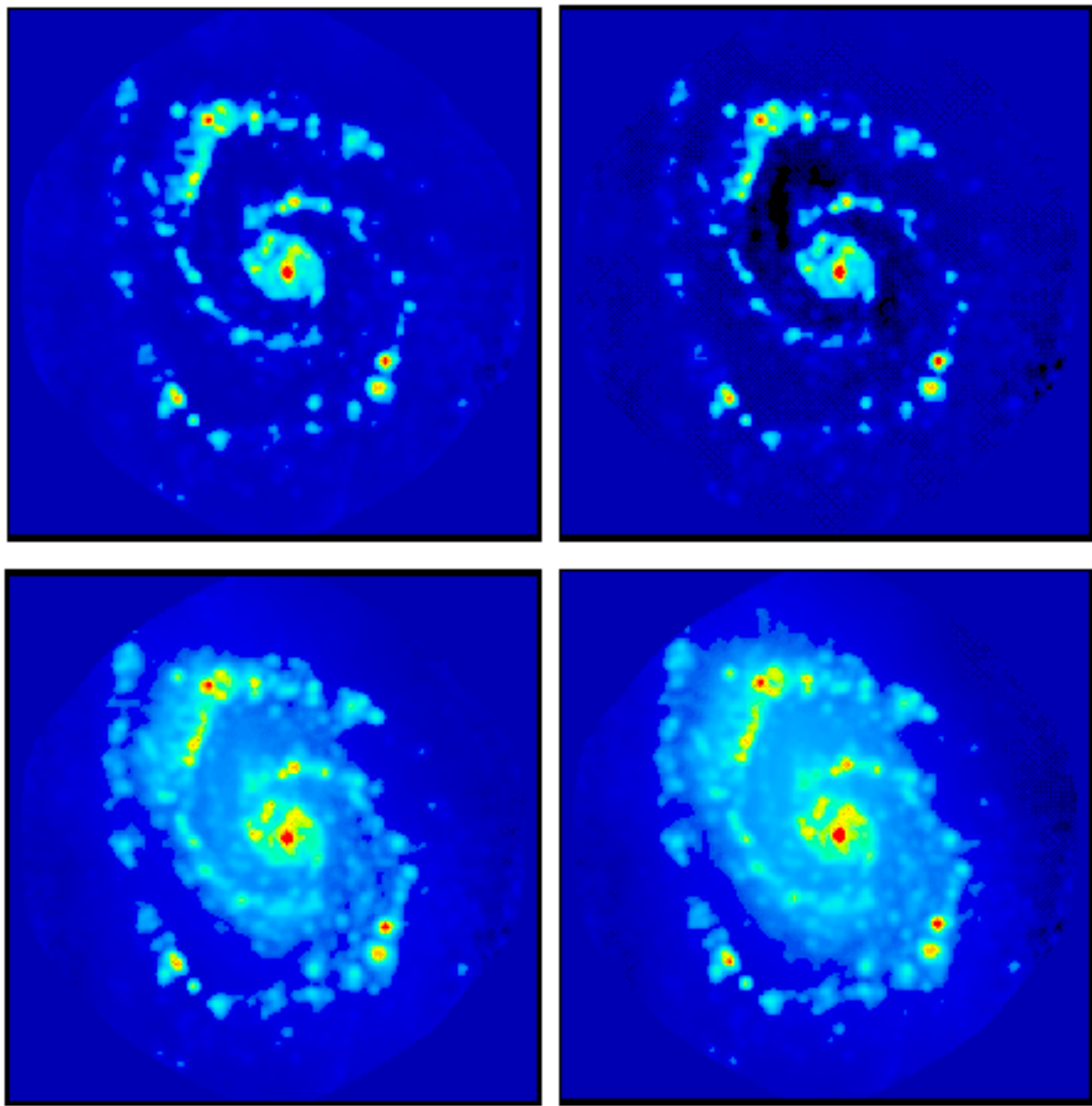


Figure 7: Simulated observations with a combined $19 \times 6\text{m}$ ACA and $64 \times 12\text{m}$ array. See Figure 3 caption for the description of each panels. The range of amplitude plotted are from -50 (black) to +350 (red).

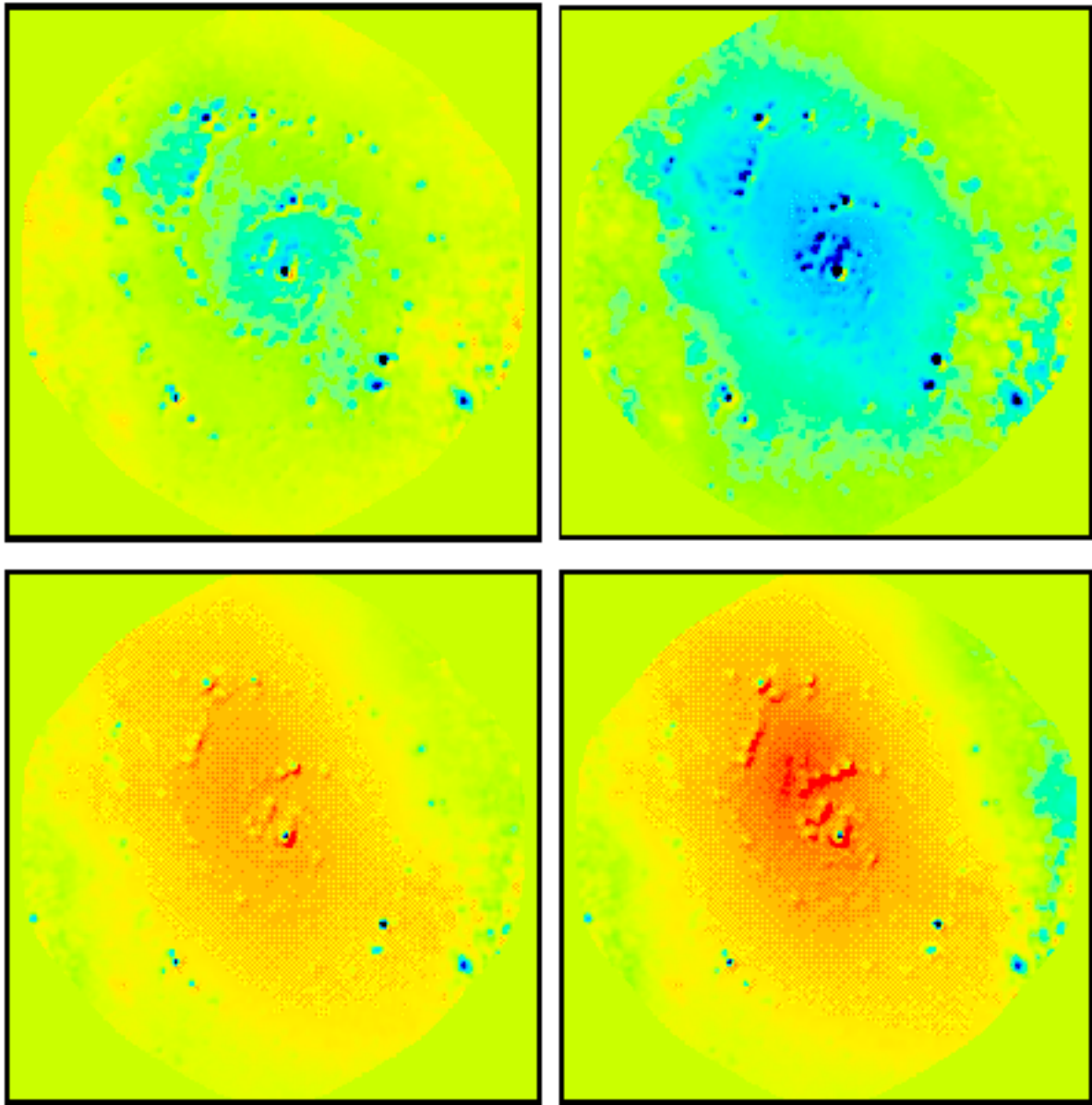


Figure 8: Difference images between the simulated observations using a combined $19 \times 6\text{m}$ ACA and $64 \times 12\text{m}$ array and the input model image convolved to the match resolution ($1''$). See Figure 4 caption for the description of each panels. The range of amplitude plotted are from -30 (black) to +30 (red).

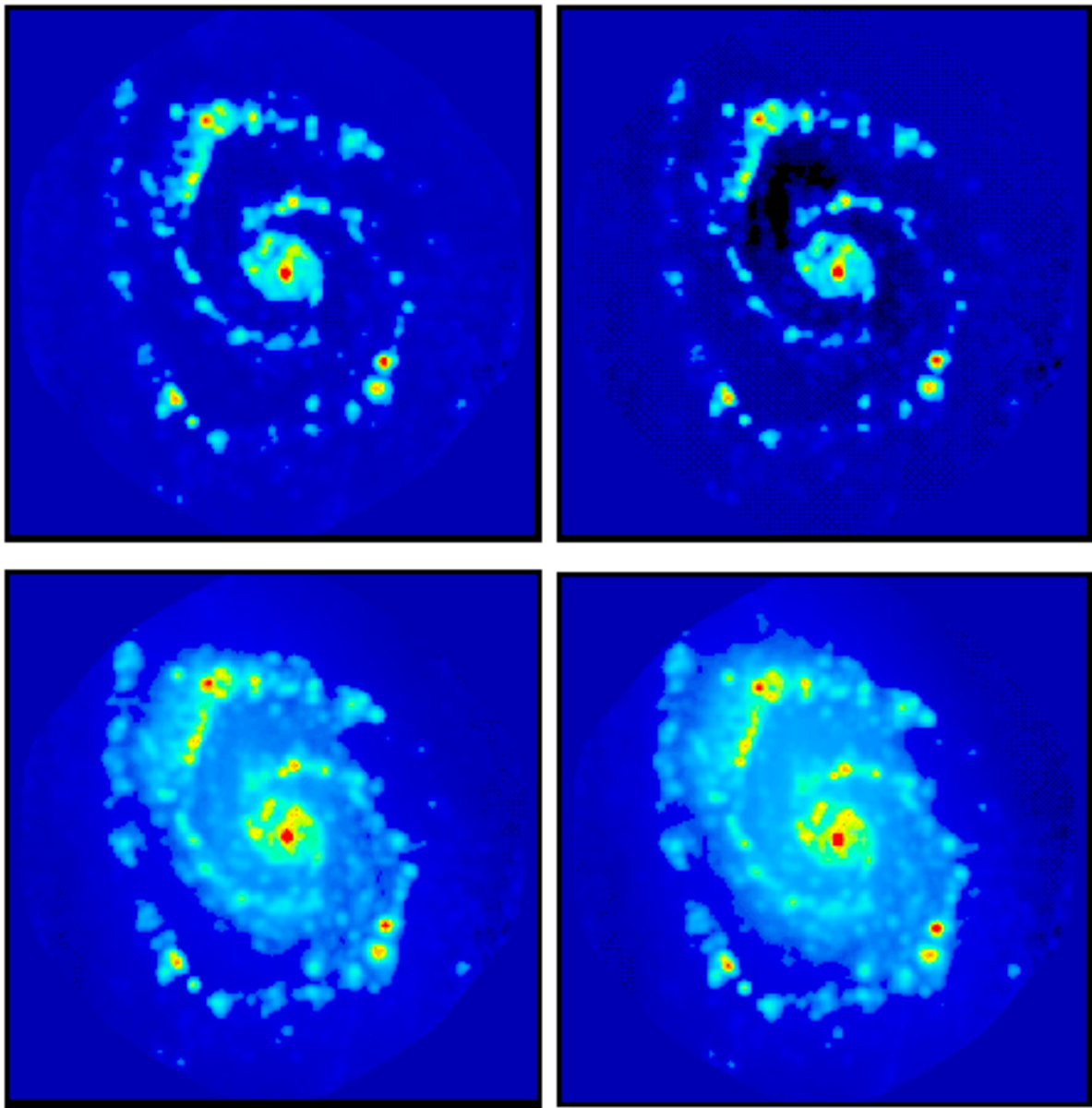


Figure 9: Simulated observations with a combined $13 \times 8\text{m}$ ACA and $64 \times 12\text{m}$ array. See Figure 3 caption for the description of each panels. The range of amplitude plotted is identical to Figure 7.

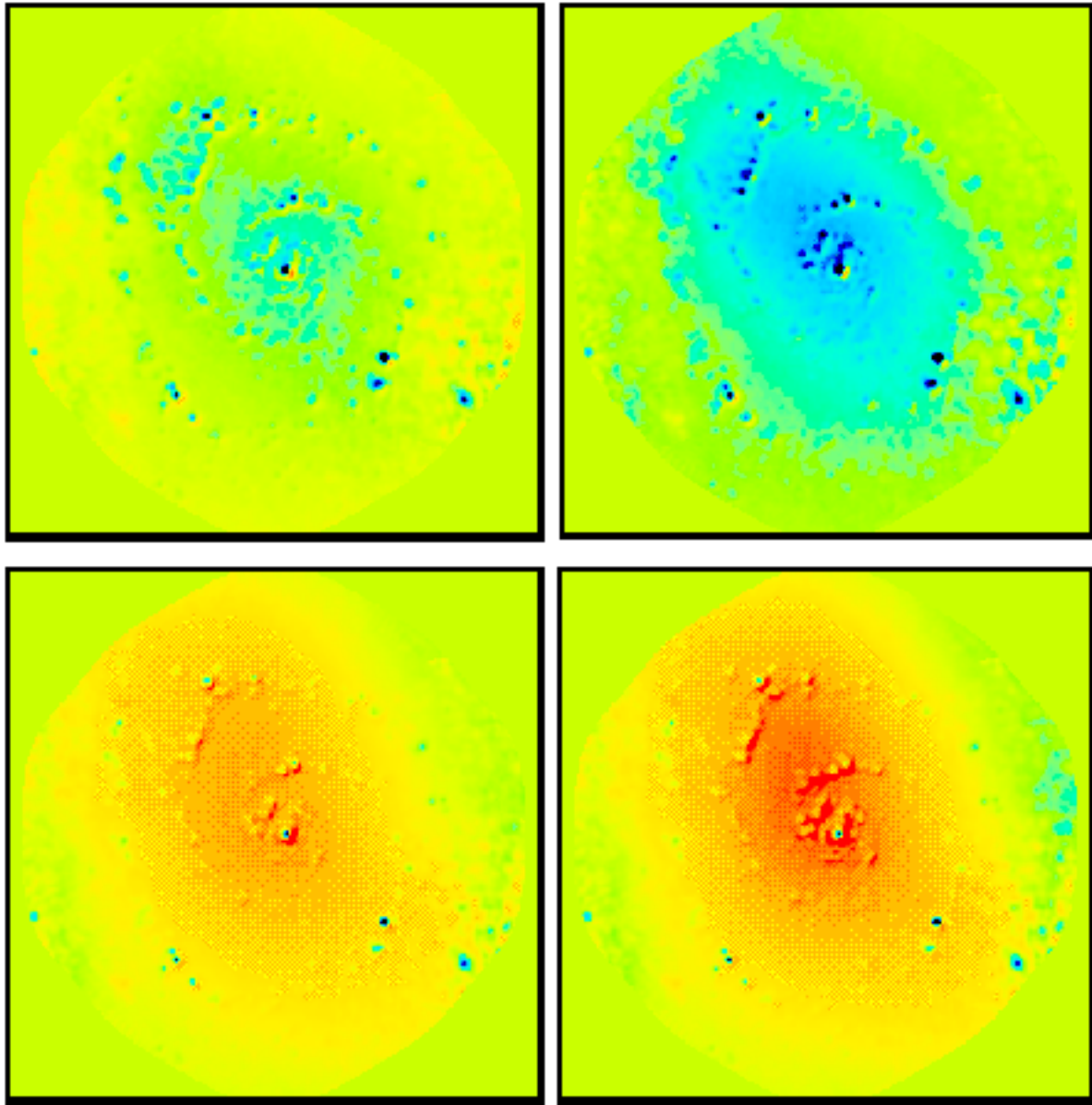


Figure 10: Difference images between the simulated observations using a combined $13 \times 8\text{m}$ ACA and $64 \times 12\text{m}$ array and the input model image convolved to the match resolution ($1''$). See Figure 4 caption for the description of each panels. The range of amplitude plotted is identical to Figure 8.

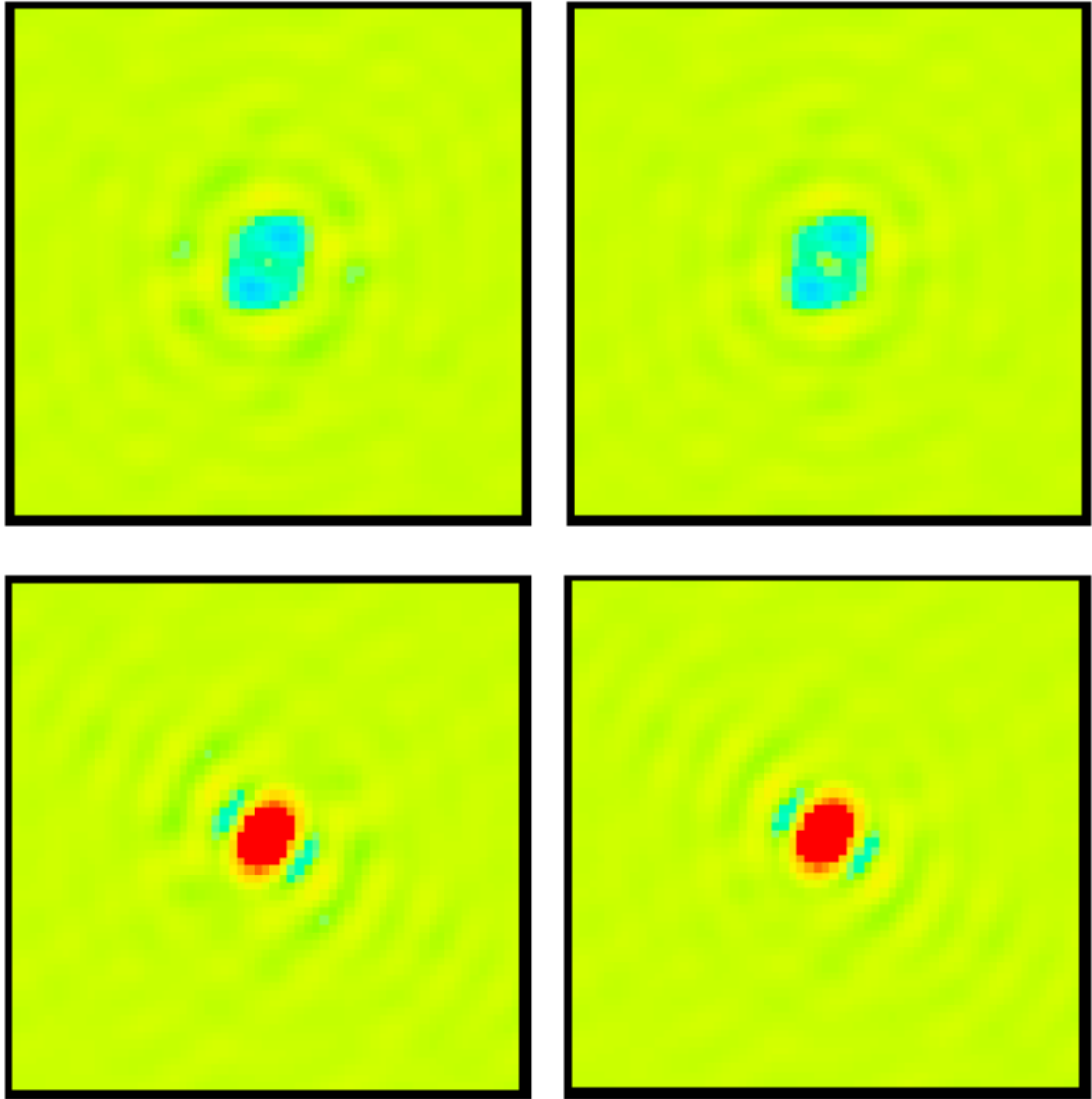


Figure 11: Greyscale representation of the real part of the Fourier transform of the difference images from VTESS (left panels of Figs. 8 & 10). Bottom and top rows are with and without the total power data, respectively. The left side panels are the 6m ACA results while the right side panels are the 8m ACA results.

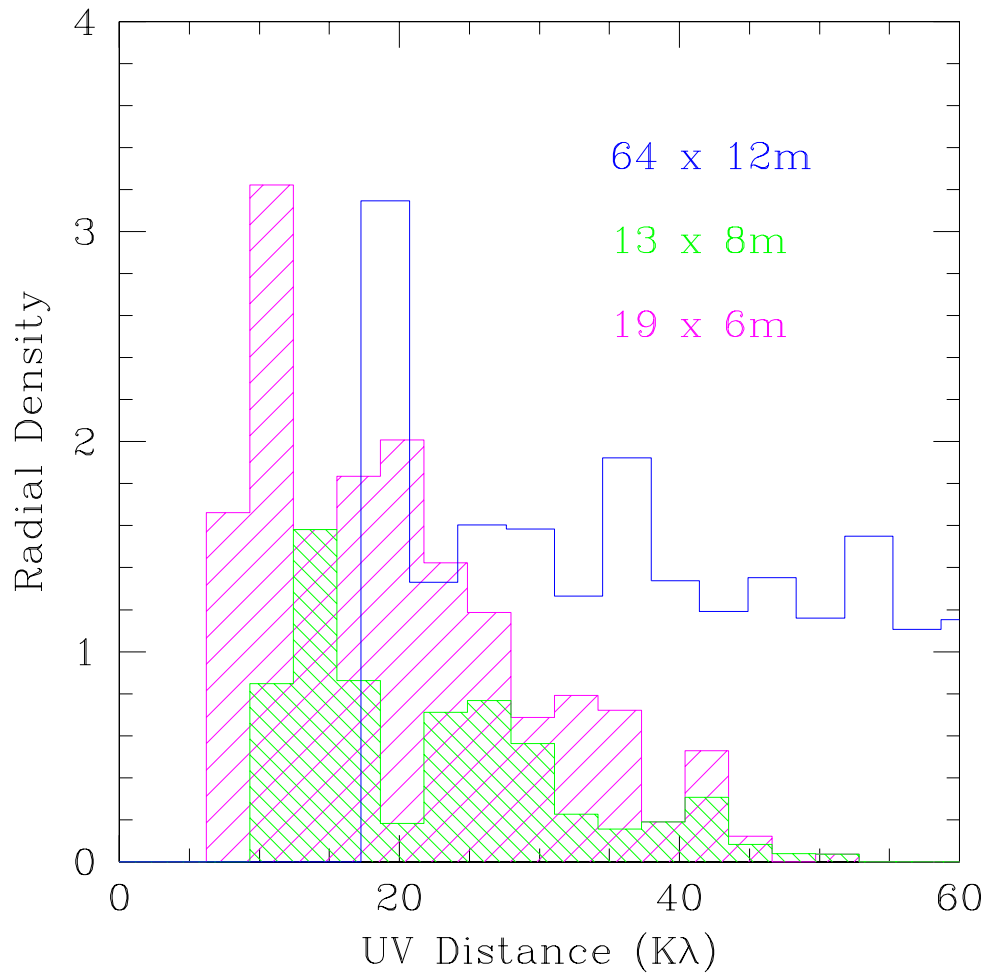


Figure 12: Plot of radial density distribution for the 6m, 8m, and 12m arrays. 10 kλ corresponds to about 8m at 345 GHz.

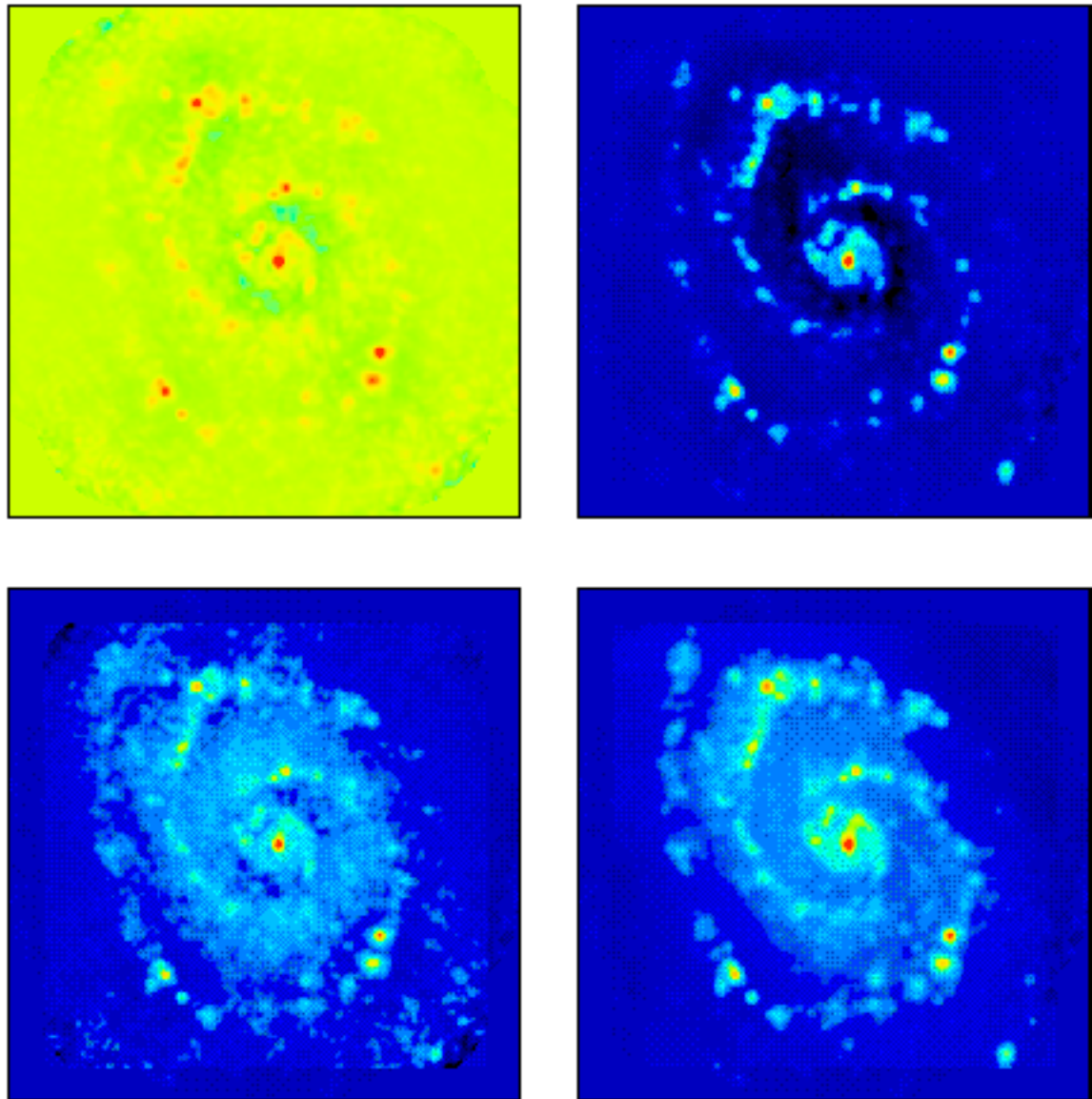


Figure 13: Simulated observations with a $64 \times 12\text{m}$ Array alone. See Figure 3 caption for the description of each panels. The range of amplitude plotted is identical to Figure 7.

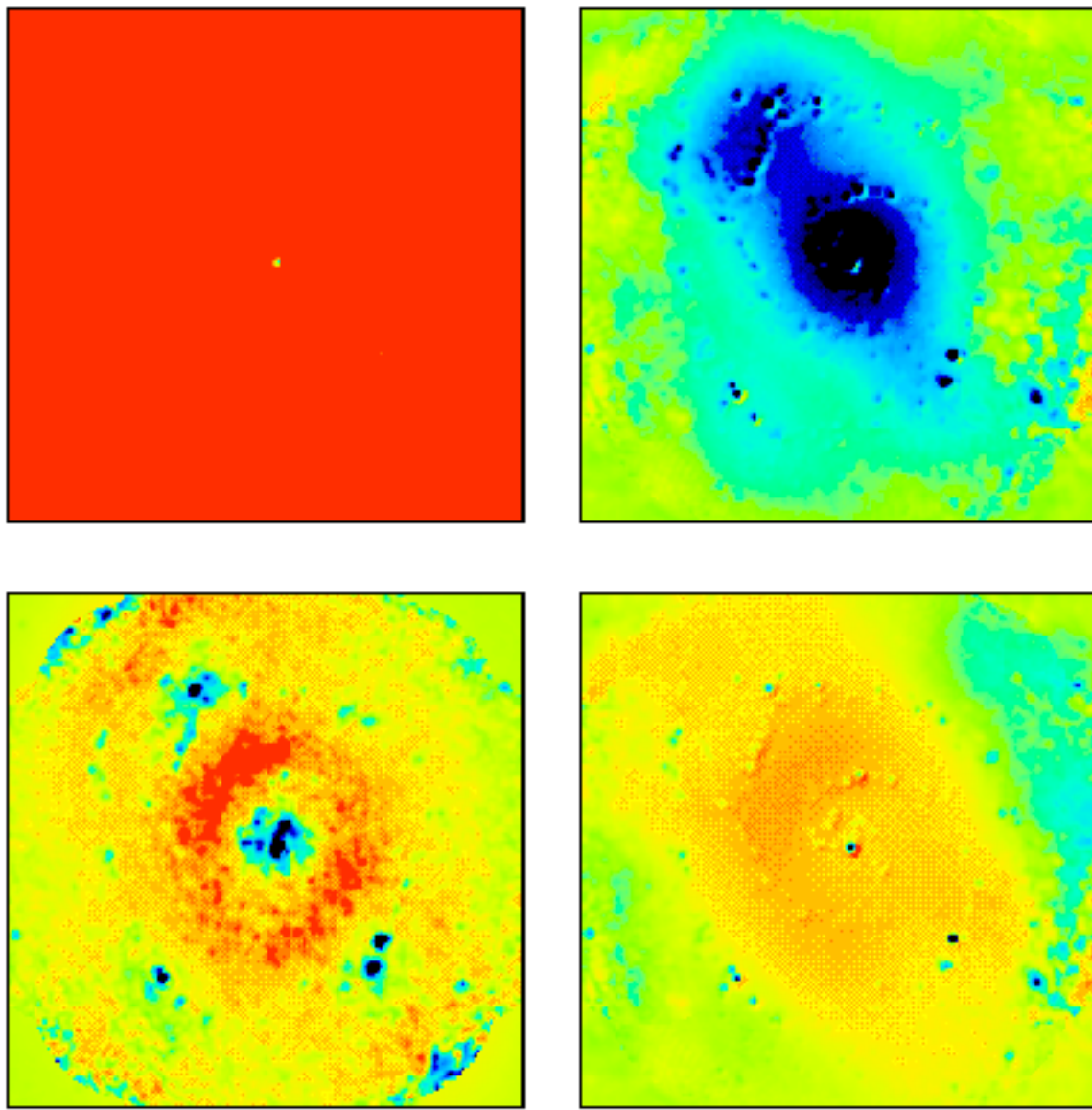


Figure 14: Difference images between the simulated observations using a 64 x 12m Array alone and the input model image convolved to the match resolution ($1''$). See Figure 4 caption for the description of each panels. The range of amplitude plotted is identical to Figure 8.

REFERENCES

- Cornwell, T. J., Holdaway, M. A., Uson, J. M. 1993, “Radio-interferometric Imaging of Very Large Objects: Implications for Array Design”, *A&A*, 271, 697
- Kogan, L. 1998, “Optimization of an Array Configuration with a Donut Constraint”, MMA Memo No. 212